Investigation of Modeling and Post-Processing Methods for Combustion Instability Experiments

By M. Wierman†, S. Beinke‡‡‡, W. Anderson†, M. Oschwald‡, M. Schulze¶, M. Zahn¶ AND T. Sattelmayer¶

† Purdue University,
West Lafayette, IN, 47907, USA
‡ German Aerospace Center (DLR) Lampoldshausen
Hardthausen, 74239, Germany
¶ Lehrstuhl für Thermodynamik, Technische Universität München
Boltzmannstr. 15, 85748 Garching b. München

This work analyzes experimental optical data and numerical results in order to investigate combustion response to high frequency acoustic disturbances. Optical data from a high frequency combustion instability experiment operated at DLR Lampoldshausen is analyzed using various decomposition analysis methods to identify the response of representative injection elements to an applied acoustic disturbance. Unsteady numerical simulations of the experimental injection elements under the influence of acoustic forcing are also simulated. The numerical results are then analyzed using the same analysis methods as the experimental data. The methods applied are used to investigate the dominant frequencies and flow structures in the experimental and numerical data. It has been shown that the decomposition analysis methods can be applied to the different data sets and identify flame behavior at the frequencies of interest.

1. Introduction

Combustion instabilities refer to a coupling between acoustic and combustion processes inside rocket engine combustion chambers. Acoustic pressure fluctuations propagate throughout a combustion chamber and interact with the combustion processes occurring therein. Under certain conditions the frequency of acoustic fluctuations may be such that mutual reinforcement occurs and self-sustaining oscillations are produced. If unimpeded, the amplitude of the fluctuations may grow to levels where it affects the operation and compromises the structure of the combustion chamber. Combustion instabilities reduce the lifetime and reliability of rocket engine combustion chambers and have the potential to cause premature failure of the rocket engine, usually resulting in loss of the rocket mission.

High frequency combustion instabilities that occur at frequencies greater than 1 kHz are the least understood and most damaging type of instability. At high frequencies the acoustic behavior is attributed to the resonant modes of the combustion chamber volume. The mechanisms which determine how combustion processes interact with and support acoustic disturbances at these frequencies are not yet understood.

‡‡ also PhD student, The University of Adelaide, Adelaide, 5000, Australia

Laboratory scale high frequency combustion instability experiments have been conducted by various research groups. The lab scale experiments are used to collect combustion instability data using instrumentation that would not be feasible in a full scale engine. The goal of such investigations is to determine which processes drive combustion instabilities and the conditions at which instabilities occur.

This work compares experimental data taken from a high frequency combustion instability experiment and numerical simulations of representative injection elements subjected to acoustic forcing. To examine the frequency content of the data, post-processing methods such as proper orthogonal decomposition (POD) and dynamic mode decomposition (DMD) are applied to both datasets using the same methodology.

The high frequency combustion instability experiment studied is a specialized combustion chamber (dubbed BKH) operated at the P8-testbench at DLR Lampoldshausen. The BKH experiment uses an acoustic excitation system to acoustically perturb a number of study elements. The response of the study elements is observed using instrumentation throughout the chamber and high speed line-of-sight imaging recorded through windows built into the sides of the chamber. High-speed imaging allows both temporally and spatially resolved measurements of the signal from combustion light and is leading to improved understanding of the spatial distribution of the combustion as a function of the unsteady amplitude.

The numerical simulations analyzed in the current work are simplified simulations of single BKH injection elements in a reduced numerical domain. The simulations are perturbed numerically by imposing a disturbance at the boundary of the numerical domain that is representative of the acoustic disturbance produced when a resonant mode is excited using the BKH excitation system. Due to the limitations of the numerical method, only longitudinal mode excitation is examined in the current work.

Optical data from the BKH experiments and flow fields from the numerical results are post-processed using decompositional methods to identify and compare flow features and frequency behavior linked to combustion instability phenomena.

2. Experimental method

The BKH combustor, shown in Figure 1, is used for high frequency combustion instability experiments. BKH operates at pressures ranging from 40 bar (sub-critical with respect to the critical pressure of oxygen) to 60 bar (super-critical with respect to the critical pressure of oxygen) using cryogenic oxygen and hydrogen propellants. The combustion chamber features a rectangular geometry with windows located on each side for optical access to the injection zone, and an acoustic excitation system consisting of a secondary nozzle and siren wheel. The combustion chamber volume is 305 mm long, 50 mm wide and 200 mm high. The rectangular geometry was designed to match the resonant mode frequencies of full-scale upper-stage rocket engines. 5 coaxial study elements arranged in a matrix pattern, as shown in figure 2, are located in the center of the chamber. The BKH excitation system is used to excite the resonant modes of the combustion chamber volume. The response of the 5 study elements to the imposed acoustic field is then observed. BKH experiments are conducted at the European Research and Technology test Facility P8 for cryogenic rocket engines at DLR Lampoldshausen. Additional BKH information can be found in Ref. [1–3]. The BKH excitation system's siren wheel is a toothed wheel positioned so that the teeth of the wheel periodically interrupt the flow through the secondary nozzle as it rotates. The rotational velocity of the

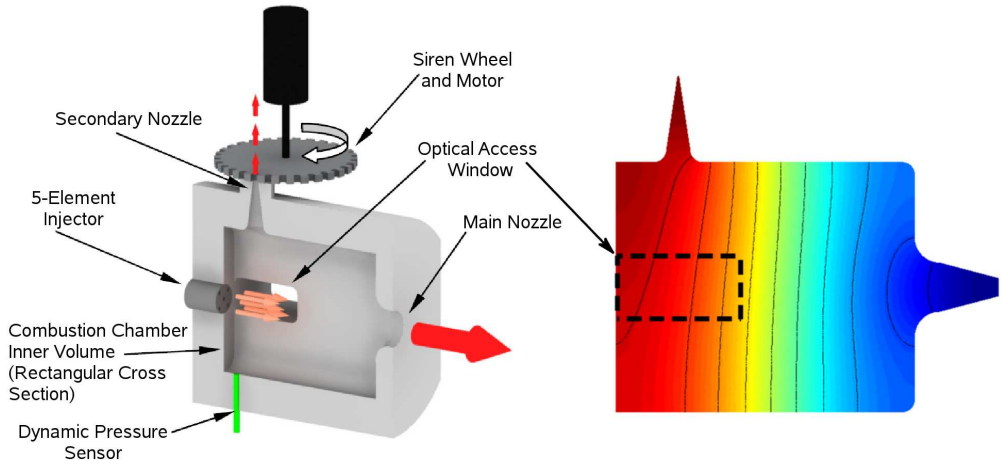

FIGURE 1. Conceptual illustration of the BKH Combustor (left) and an estimated BKH 1L mode showing window region (right).

siren wheel determines the frequency of the applied disturbance. During an experiment the excitation frequency is steadily ramped through a range of frequencies to excite the resonant modes of the chamber. The secondary nozzle is oriented perpendicularly to the main flow direction and is therefore more suited for excitation of transverse acoustic modes. With the excitation system, BKH experiments have recorded acoustic pressure fluctuation amplitudes greater than 9% of the mean chamber pressure when exciting at the resonant frequency of the chamber.

Samples from 2 BKH experiments are analyzed in the current work. The data samples have been taken from periods when the excitation frequency was near or at the first longitudinal mode (1L) frequency. An estimated BKH 1L mode shape is shown in figure 1. During 1L mode excitation the window and injection elements are located in a pressure anti-node.

The operating conditions for each data sample are described in table 1. The combustion chamber pressure for both samples is greater than 60 bar which is higher than the critical pressure of oxygen (50.43 Bar). Cryogenic liquid oxygen is injected at temperatures below the critical temperature of oxygen (154.59 K) and therefore undergoes transcritical injection as it is quickly heated above the critical temperature upon entering the chamber. The oxidizer to fuel ratio (ROF) of the study elements is approximately 6 which is similar to that of full scale engines which operate in an ROF range between 4.5 and 7.2. The BKH chamber operates with a large amount of secondary hydrogen injection. This secondary injection is used to protect the optical windows from the high temperatures of the flame zone and prevent strong recirculation above and below the study elements. The secondary hydrogen injection also reduces the mean ROF of the BKH chamber.

The experimental data analyzed in the current work consists of pressure data, frequency data, and optical data. Dynamic pressure sensor data is sampled at a rate of 100 kHz from a sensor mounted in the wall opposite to the secondary nozzle as shown in figure 1. These data are used to observe the acoustic field inside the BKH chamber. The excitation frequency can be extracted by analysing the pressure data. It is also

Operating Condition	Test 1	Test 2
Combustion chamber pressure (bar)	62.0	60.6
Hydrogen mass flow rate (g/s)	106	94
Oxygen mass flow rate (g/s)	569	567
Secondary hydrogen mass flow rate (g/s)	1170	1142
Hydrogen temperature (K)	293	297
Oxygen temperature (K)	127	125
Secondary hydrogen temperature (K)	294	297
ROF study elements	5.37	6.04
ROF mean chamber	0.507	0.522
Excitation frequency ramp rate (Hz/s)	167	84

TABLE 1. BKH experimental data sample operating points.

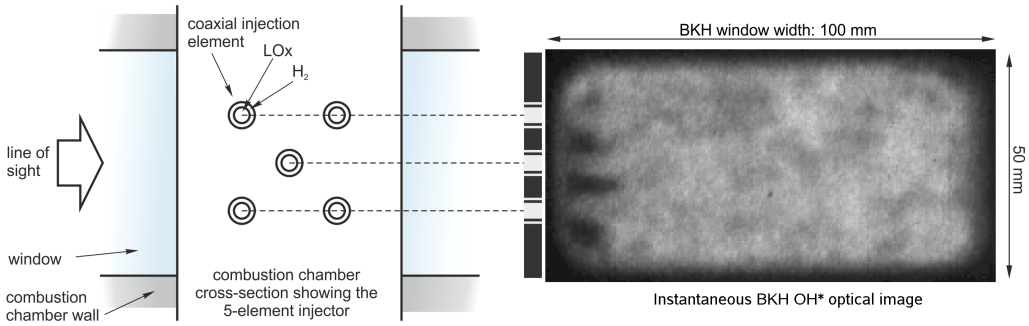

FIGURE 2. BKH study element configuration and optical data.

measured by a tooth detector that detects the teeth of the siren wheel as it rotates. The tooth detector output is then filtered to determine the excitation frequency.

The optical data consists of line-of-sight OH* chemiluminescence imaging recorded through the optical windows in the sides of the chamber during BKH experiments. OH* chemilimunescence is used to study reaction zones of oxygen-hydrogen flames. The hydroxyl radical OH* becomes excited during combustion and emits a photon as it decays. As this excitation and emission process is very fast, OH* emission is used as an indicator of the relative heat release rate in oxygen-hydrogen flames. The optical windows are 10cm wide $\times$ 5cm high and positioned to observe the near injector region about the 5 study elements as described in figure 2. A Photron FASTCAM APX-i2 intensified camera is used to record high-speed images at a sampling rate of 24,000 frames per second (fps) and a resolution of 256$\times$128 pixels. An OH* filter with a wavelength pass band of 305 $\pm$ 5nm is used to record OH* emission. An optical data image is shown in figure 2. Due to the line of sight optical access only 3 of the 5 injection elements are directly observed in the recorded data.

3. Numerical method

2-dimensional axis-symmetric simulations of single BKH injection elements subjected to an acoustic disturbance were computed in the frame of the summer program. This simplified approach was used to reduce the computational requirements and complexity of the simulations. Only the case corresponding to test 2 in table 1 has been simulated.

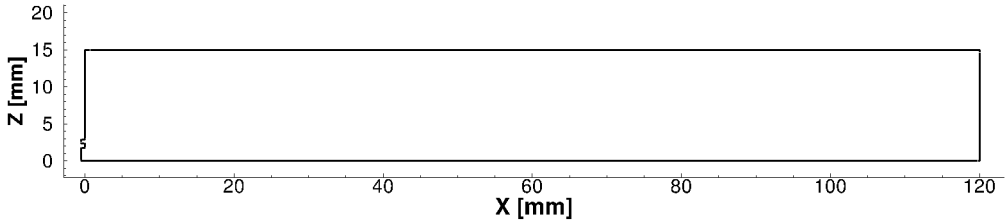

FIGURE 3. Numerical domain used for DLR TAU code simulations.

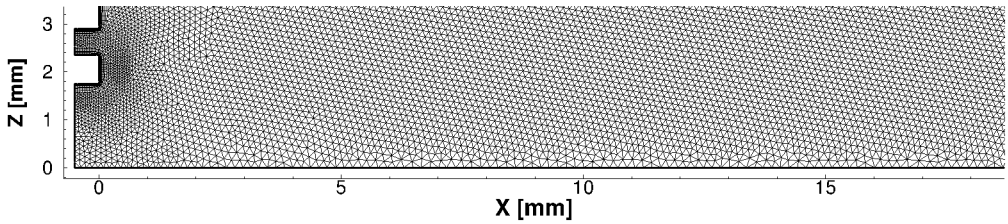

FIGURE 4. Close up view of DLR TAU code mesh near injection plane.

Results were produced using two CFD codes: the DLR TAU code, and the commercial software ANSYS CFX. The method and results from each code are presented in the following sections.

3.1. *DLR TAU code simulations*

The DLR TAU-code is a hybrid structured/unstructured second order finite-volume flow solver for the compressible Euler and Navier-Stokes equations in the integral form. It has been validated for a range of steady and unsteady flow cases [4, 5]. Turbulence models ranging from RANS one and two equation models to detached and large eddy simulations have been implemented in TAU. For the current work the one-equation Spalart-Allmaras [7] turbulence model was used.

Karl and Lüdeke [6] validated the TAU-code for acoustic damping cavities. They employed the AUSMPUP upwind solver which is an extension of the AUSM+ scheme. A Jameson-type dual time stepping scheme was used for unsteady calculations. A MAPS+ upwind solver with the Thornber modification [9] is used to conduct unsteady RANS simulations in the current work. The same Jameson-type dual time stepping method with 100 inner iterations per outer time step was also used.

The fluid is treated as a reacting mixture of perfect gases. A finite rate chemistry scheme that solves the Arrhenius equation is used in the current work. The mechanism is described by Gerlinger [8] and consists of 8 species and 19 reactions.

A reduced 2-dimensional axis-symmetric domain containing a single BKH injection element was chosen. The size of the computational domain was chosen based on initial investigations to ensure the flame zone remained within the domain. The domain was meshed with a hybrid grid consisting of approximately 50,000 points. The computational domain and grid is shown in figures 3 and 4.

Dirichlet boundary conditions were prescribed at the propellant inlets to the numerical domain. To accommodate the perfect gas assumption the injection conditions were modified to satisfy the ideal gas equation of state. Table 2 lists the prescribed injection conditions. The perfect gas assumption does not significantly affect the hydrogen injection conditions however the dense liquid oxygen core cannot be captured. For the DLR

Hydrogen Temperature (K)	297
Hydrogen Density (kg/m^3)	4.89
Hydrogen Velocity (m/s)	423
Oxygen Temperature (K)	125
Oxygen Density (kg/m^3)	184.75
Oxygen Velocity (m/s)	63.794

TABLE 2. DLR TAU code simulation injection conditions.

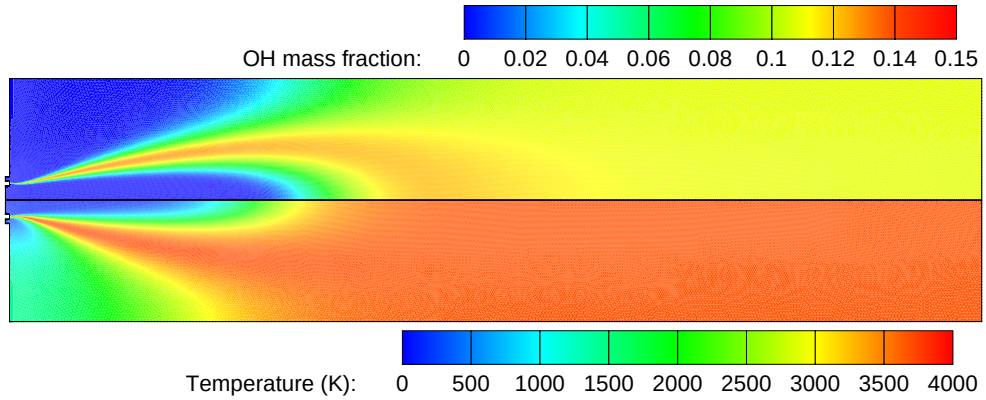

FIGURE 5. DLR TAU code steady state flow field results.

TAU simulations the injection temperature matched the experiment, leading to significantly smaller density being prescribed than the experimental value as listed in table 1. To maintain the correct mass flow of oxygen into the chamber, the injection velocity is increased. This allows the mass flow of propellants to be preserved but also changes the momentum ratio between the hydrogen and oxygen streams. The center line of the injection element was treated as an axis-symmetric boundary.

The top and right boundaries in figure 3, which do not represent a physical wall but rather internal fluid boundaries, were prescribed with "near-field" boundary conditions. A state is specified at the near field boundary and the flux across the boundary is determined by the difference between this state and the interior points in the numerical domain. This boundary condition was used as it allowed a fluid state at a specified pressure to be prescribed along a large portion of the boundary of the numerical domain, effectively setting the mean pressure across the domain. The near-field boundaries were prescribed to match the combustion chamber pressure specified in 1. All other boundaries were prescribed to be slip walls.

A steady state RANS solution was first computed as shown in figure 5. The steady state solution was used as the initial condition for the unsteady RANS computation.

An unsteady RANS simulation using a time step of 5×10^{-7} was computed. The near-field boundary conditions described previously were modified after each time step to impose a fluctuating acoustic pressure. A sinusoidal pressure fluctuation at the target BKH 1L mode frequency of 3200 Hz and amplitude of 1 bar was imposed to match the 1L mode observed experimentally. An unsteady simulation was computed for a total time of 3 ms. The initial disturbance transient during the first 0.5 ms was discarded

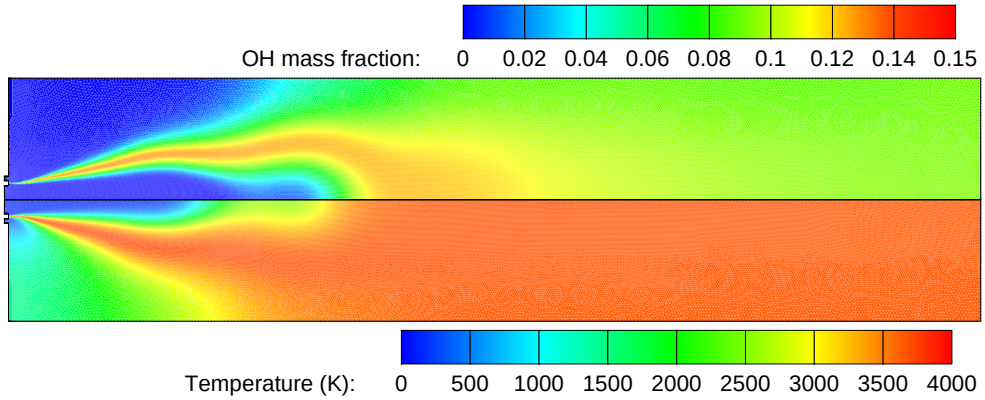

FIGURE 6. DLR TAU code instantaneous unsteady flow field results at t=2.765 ms.

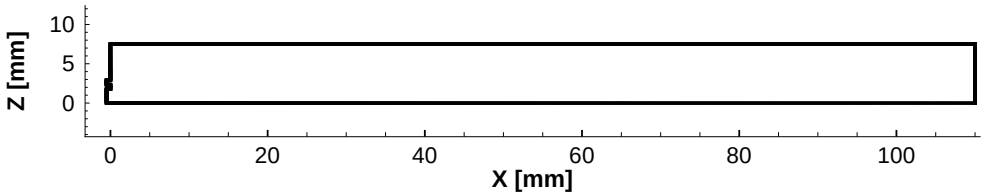

FIGURE 7. Numerical domain used for ANSYS CFX simulations.

leaving a period of 2.5 ms of unsteady numerical data exhibiting steady oscillations for approximately 8 acoustic pressure periods. The instantaneous perturbed flow field after a number of cycles is shown in figure 6.

3.2. *ANSYS CFX simulations*

Unsteady simulations of a single BKH injector were performed using an approach previously described in [19, 21]. Unsteady RANS simulation with $k-\epsilon$ turbulence modelling and an Eddy Dissipation Model to account for the combustion process were computed with the commercial solver ANSYS CFX and the system is excited in the frequency range of interest. The global reaction $\frac{1}{2}O_2 + H_2 \rightarrow H_2O$ is used in the Eddy Dissipation Model. All species were modeled as ideal gases.

A 2D axis-symmetric domain was used with a grid of approximately 50,000 points. The Computational domain was rectangular with a height of 7.5 mm and a length of 100 mm. This size was chosen to match the length of the window region and the spacing between coaxial elements in the center of the chamber. The face plate and outer wall of the domain were treated as slip walls and the inner wall as an axis-symmetric boundary. The remaining side of the numerical domain was treated as an outlet at a fixed pressure to match the specified chamber pressure. Constant mass flows of the propellants at their respective injection temperatures were applied at the injector locations. The computational domain and grid are shown in figures 7 and 8.

The acoustic perturbation at the frequency of interest was imposed using source terms of mass with the local composition of the calculated species. The source terms were used to add or remove mass periodically from the numerical domain to represent the acoustic perturbation. The amount of mass injected was varied along the length

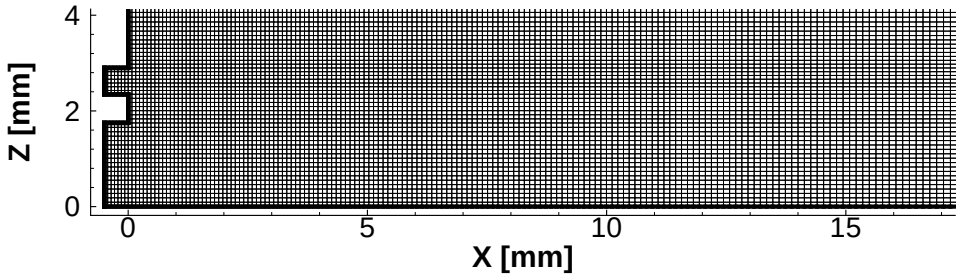

FIGURE 8. Close up view of ANSYS CFX mesh near injection plane.

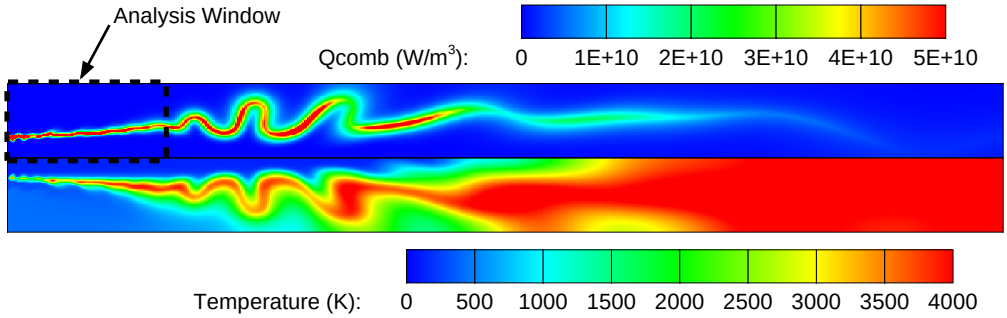

FIGURE 9. CFX instantaneous unsteady flow field results and analysis window.

of the domain to apply a pressure disturbance that varied over the longitudinal direction. Hence the disturbance imposed is more representative of a longitudinal mode. The pressure out the outlet boundary was also modulated to match the disturbance. The resultant flow field after a number of pressure cycles is shown in figure 9. OH species are not considered in the single step chemistry model used for the CFX simulations. The heat release $Qcomb$ will be used to compare with the experimental OH* data.

4. Post-processing methods

Meaningful processing of large quantities of data from experimental and numerical sources requires automated, orderly computational processing to properly analyze and isolate significant behaviors. Proper Orthogonal Decomposition (POD) and Dynamic Mode Decomposition (DMD) have been investigated for such processing due to their spatially and temporally resolved output of orthogonal basis functions or modes. POD decomposes data based on decreasing modal singular values as an indicator of the magnitude of the descriptivity of the unsteady processes in each mode. DMD decomposes data into orthogonal modes based on frequency, which can be especially useful for data with specific acoustic modes as in combustion instability. These techniques are applied to the output from the experimental results and numerical simulations of the BKH combustor in 1L excitation. [16–18, 22]

(a) Spatial Component for numerical domain (Fig. 3)

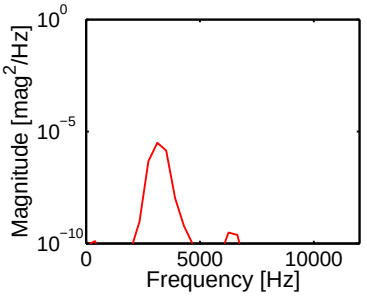

(b) PSD of Temporal Component

FIGURE 10. POD Mode 1 information for BKH TAU OH Mass Fraction simulation data.

5. Results

5.1. *POD Analysis*

5.1.1. *TAU Results*

POD was applied to the TAU code unsteady OH mass fraction data. The numerical OH mass fraction was analyzed as the closest available comparison to the experimental OH* emission data. The spatial component of POD mode 1 (Fig. 10(a)) shows a distribution of paired oppositely signed regions along the mean flow path of the injector. The power spectral density of the corresponding temporal component (Fig. 10(b)) shows a prominent peak at 3200Hz and the next harmonic at 6400 Hz. This matches the driven pressure excitation exactly. POD Mode 2, not shown here, has similar spatial and temporal character but shifted in space and time. The result between the two POD modes is a pulsing unsteady response at the disturbance frequency along the mean flow direction. The local pressure perturbation causes a fluctuation in the diameter of the oxygen jet and flame which propagates downstream.

5.1.2. *CFX Results*

POD was applied to the CFX unsteady heat release data. The heat release data was analyzed as the closest available comparison to the experimental OH* emission data. The spatial component of POD mode 1 (Fig. 11(a)) shows a single pair of oppositely signed regions along the mean flow path of the injector, unlike the multiple regions from the TAU results (Fig. 10(a)). The power spectral density of the corresponding temporal component (Fig. 11(b)) shows a prominent peak at 3233Hz and the next harmonic at 6445 Hz. This matches the driven pressure excitation within the resolution of the PSD. POD Modes 2 and 3 (not pictured) show similar spatial and temporal character but shifted in space and time. As with the TAU POD analysis (Fig. 11), the result from the three POD modes is a pulsing unsteady response at the disturbance frequency along the mean flow direction. The local pressure perturbation causes a fluctuation in the diameter of the oxygen jet and flame which propagates downstream.

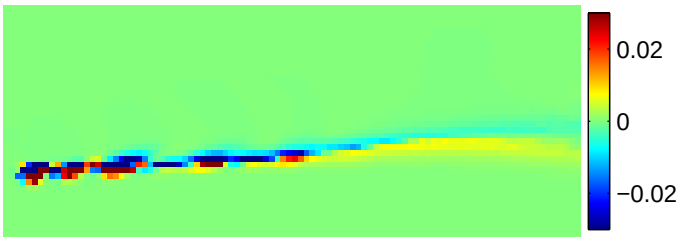

(a) Spatial Component for analysis window (Fig. 9)

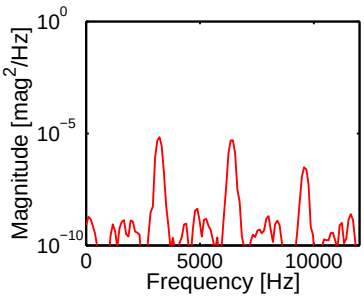

(b) PSD of Temporal Component

FIGURE 11. POD Mode 1 information for BKH CFX Heat Release simulation data.

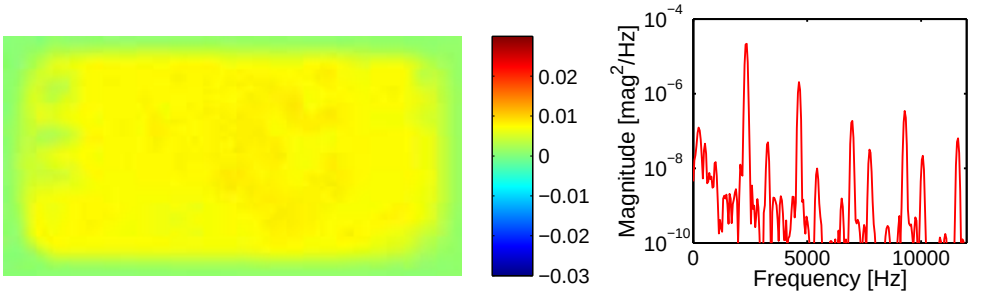

(a) Spatial Component for entire window region (Fig. 2) (b) PSD of Temporal Component

FIGURE 12. POD Mode 1 information for BKH OH^* emission experimental data.

5.1.3. *Experimental Results*

POD was applied to short samples of BKH OH* optical data during periods of steady pressure amplitudes. The POD Mode 1 spatial component (Fig. 12(a)) shows a region of almost uniform and single signed response. As the first POD Mode, this is the most descriptive mode of the unsteady behavior of the OH* data. The power spectral density of the corresponding temporal component (Fig. 12(b)) shows significant peaks at 2300Hz and its harmonics along with less prominent peaks at 3200Hz and its harmonics. The peaks associated with 3200Hz are related to the direct excitation from the secondary nozzle and toothed wheel. The peaks associated with 2300Hz are from a persistent camera artifact that is attributed to a coupling between the image intensifier and high speed camera used to record the data. The camera artifact is present in all available BKH OH* high speed optical data. The artifact occurs at specific frequencies, and its magnitude is larger than any observed response of the flame. The magnitude of the artifact is also believed to be dependent on the incoming light intensity, meaning it can

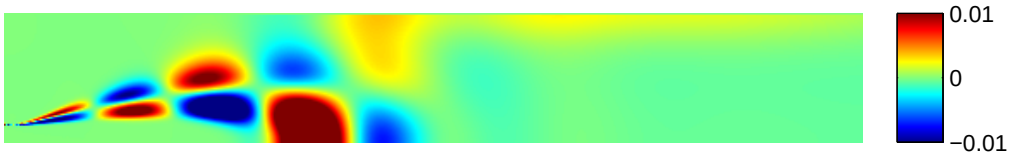

FIGURE 13. DMD spatial mode at 3200 Hz for BKH TAU OH Mass Fraction simulation data for numerical domain (Fig. 3).

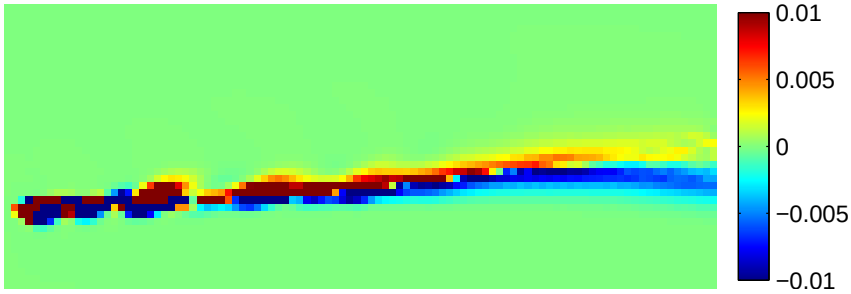

FIGURE 14. DMD spatial mode at 3267 Hz for BKH CFX Heat Release simulation data for analysis window (Fig. 9).

not be filtered or removed from the optical data with ease. POD analysis of all tests and time slices were dominated by the artifact. Therefore successive POD modes were not able to resolve other notable frequency content. Due to the artifact, POD was deemed unsuitable for analysis of the BKH OH* optical data.

5.2. *DMD Analysis*

5.2.1. *TAU Results*

DMD was applied to the same TAU code unsteady OH mass fraction data as the POD. The spatial component of the DMD mode at 3200Hz (Fig. 13) shows a distribution of paired oppositely signed regions along the mean flow path of the injector. The 3200Hz DMD mode had the most prominent peak in frequency distribution, marking the most descriptive behavior and matching the numerically imposed excitation frequency. This matches the behavior seen in the corresponding POD analysis of the TAU results (Fig. 10(a)). Both are resolving the response to the driven pressure excitation.

5.2.2. *CFX Results*

DMD was applied to the CFX unsteady heat release data. The spatial component of the DMD mode at 3267Hz (Fig. 14) shows a single pair of oppositely signed regions along the mean flow path of the injector, which is nearly identical to the distribution from the corresponding POD analysis (Fig. 11(a)). The 3267Hz DMD mode had the most prominent peak in frequency distribution, marking the most descriptive behavior and matching the numerically imposed excitation frequency within the resolution of the DMD. As with the POD analysis (Fig. 10), behavior from this mode is a pulsing unsteady response at the disturbance frequency along the mean flow direction.

5.2.3. *Experimental Results*

DMD was applied to the same experimental data samples of OH* emission data as described in section 5.1.3. The spatial component of the resultant DMD mode at 3233Hz

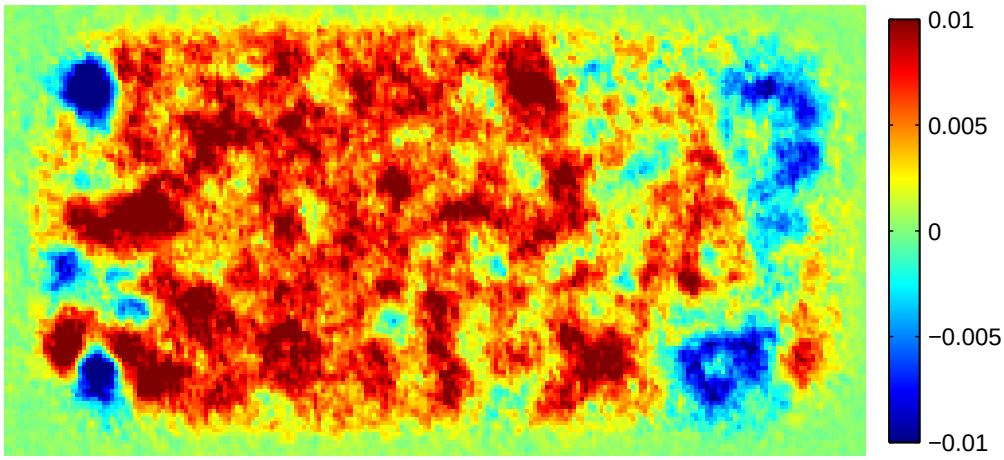

FIGURE 15. DMD spatial mode at 3233 Hz for BKH OH^* emission experimental data for window region (Fig. 2). Flow is from left to right.

(Fig. 15) shows a broad region of near constant value fluctuation in the region downstream of the injectors. The near injector region shows strong response with the same sign at the location of each study element in comparison with figure 2. The three visible study elements have the same sign as the downstream region and exhibit a higher magnitude response. The small region in between each study element has an opposite sign response. The 3233Hz DMD mode had the most prominent peak in frequency distribution for this time slice, marking the most descriptive behavior and nearly matching the driven excitation frequency.

6. Discussion

A response to the numerically imposed acoustic disturbance was revealed using both POD and DMD analysis of the numerical results. The response to the acoustic disturbance observed numerically mostly consisted of a fluctuation in the jet diameter as the propellants traveled downstream. The OH mass fraction and heat release rate also increased during the high pressure part of the cycle, and as the flame was wrinkled to increase its surface area, indicating this could be a feedback mechanism for combustion instability phenomena. The POD and DMD methods successfully identified these fluctuations and their locations within the numerical domain over time.

Both numerical approaches produced qualitatively similar results. The ANSYS CFX results agreed better with experimental observations of the liquid oxygen core length. The DLR TAU code results observed a significantly shorter oxygen core length and reaction zone. This may be due to the different turbulence models and more reaction mechanisms applied. The ideal gas assumption used in both approaches may also be significant for capturing breakup of the dense liquid oxygen core.

The DMD analysis of the experimental data revealed a uniform response in the window region near the excitation frequency. Since the excitation frequency was known from other measurements the correct DMD mode could be identified and studied. DMD analysis was therefore more suitable for analysis of the BKH data than POD which was greatly affected by the camera artifact.

The DMD of the experimental results indicate a uniform response downstream of

injection which was not directly visible in the numerical results. There is a clear limitation in the comparison of these results. The experimental images are of line-of-sight OH* emission of multiple overlapping flames. The numerical results are axis-symmetric slices of OH mass fraction. 3D turbulent structures and interaction between study elements cannot be captured with the 2D numerical models being employed. In the future, the numerical results could be further post-processed to estimate the line-of-sight response, or 3D simulations could be computed.

7. Conclusion

High speed optical data and results from representative numerical simulations have been processed and analyzed using POD and DMD methods. The concurrent decomposition analysis of experimental and numerical results provides a more rigorous means of comparison and validation than lower-order means such as separately comparing frequency, amplitude, and mode shape. The decomposition analysis was able to identify dominant frequencies and spatial structures that are not readily observable in the raw data.

This comparison of numerical and experimental results serves as a first iteration at an ongoing concurrent analysis of experiments and numerical simulations. Future improvements will allow better direct comparisons between experimental and numerical data.

Acknowledgments

The authors would like to thank Justin Hardi for helpful conversations and management of the BKH experiments, along with Dimitry Suslov, Phillip Gross, and the members of the P8 test bench. Further thanks to Sebastian Karl, Volker Hannemann, and Daniel Banuti from the Aerodynamics and Flow Technology group at DLR Göttingen for the TAU code support and expertise provided. The authors also like to thank Martin Schmid from the Institute of Thermodynamics, TUM., for assistance producing the CFX data, and Dr. Christian Stemmer, Sandra Boelk, and the SFB-TRR Program for this opportunity.

Research undertaken for this report has been assisted with a grant from the Sir Ross and Sir Keith Smith Fund (Smith Fund) (www.smithfund.org.au). The support is acknowledged and greatly appreciated. The Smith Fund by providing funding for this project does not verify the accuracy of any findings or any representations contained in it. Any reliance on the findings in any written report or information provided to you should be based solely on your own assessment and conclusions. The Smith fund does not accept any responsibility or liability from any person, company or entity that may have relied on any written report or representations contained in this report if that person, company or entity suffers any loss (financial or otherwise) as a result.

Research was also supported by the NASA Space Technology Research Fellowship.

References

[1] HARDI, J., BEINKE, S., OSCHWALD, M. AND DALLY, B. (2012). Coupling Behaviour of Lox/H2 Flames to Longitudinal and Transverse Acoustic Instabilities. In: *48th AIAA/ASME/SAE/ASEE Joint Propulsion Conference & Exhibit*, Atlanta, Georgia.

[2] HARDI, J. (2012). *Experimental Investigation of High Frequency Combustion Instability in Cryogenic Oxygen-Hydrogen Rocket Engines*. Ph.D. thesis, The University of Adelaide.

[3] HARDI, J., OSCHWALD, M. AND DALLY, B. (2013). Acoustic characterization of a rectangular rocket combustor with liquid oxygen and hydrogen propellants. *Proceedings of the Institution of Mechanical Engineers, Part G: Journal of Aerospace Engineering*, **227**(3), 431–441.

[4] GERHOLD, T., FRIEDRICH, O., EVANS, J. AND GALLE, M. (1997). Calculation of Complex Three-Dimensional Configurations Employing the DLR-TAU-Code. *AIAA paper 97-0167*.

[5] MACK, A. AND HANNEMANN, V. (2002). Validation of the unstructured DLR-TAU-Code for Hypersonic Flow. *AIAA paper 2002-3111*.

[6] KARL, S. AND LÜDEKE, H. (2008). *Application of the DLR TAU code to predict acoustic damping rates in generic combustion chamber configurations*. DLR IB 224-2012-A67

[7] SPALART, P. R. AND ALLMARAS, S. R. (1992). A One-Equation Turbulence Model for Aerodynamic Flows. *AIAA paper 92-0439*.

[8] GERLINGER, P. (2003). Investigation of an assumed pdf approach for finite rate chemistry. *Combustion Science and Technology*, **175**, 841–872.

[9] THORNBER, B., MOSEDALE, A., DRIKAKIS, D., YOUNGS, D. AND WILLIAMS, R. J. R. (2008). An improved reconstruction method for compressible flows with low Mach number features. *Computational Physics*, **227**, 4873–4894.

[10] PALIS. P., DUROX, D., SCHULLER, T. AND CANDEL, S. (2011). Nonlinear combustion instability analysis based on the flame describing function applied to turbulent premixed swirling flames. *Combustion and Flame*, **158**, 1980–1991.

[11] BELLOWS, B., BOBBA, M., SEITZMAN, J. AND LIEUWEN, T. (2007). Nonlinear Flame Transfer Function Characteristics in a Swirl-Stabilized Combustor. *Journal of Engineering for Gas Turbines and Power*, **129**, 954–961.

[12] HIELD, P., BREAR, M. AND JIN, S. (2009). Thermoacoustic limit cycles in a premixed laboratory combustor with open and choked exits. *Combustion and Flame*, **156**, 1683–1697.

[13] CULICK, F. (1987). A Note on Rayleigh's Criterion. *Combustion Science and Technology*, **56**, 159–166.

[14] THUMULURU, S., MA, H. AND LIEUWEN, T. (2007). Measurements of the Flame Response to Harmonic Excitation in a Swirl Combustor. In: *45th AIAA Aerospace Sciences Meetings and Exhibit*, Reno, NV.

[15] PAPARIZOS, L. AND CULICK, F. (1986). The Two-Mode Approximation to Nonlinear Acoustics in Combustion Chambers I. Exact Solution for Second order Acoustics. *Combustion Science and Technology*, **65**, 39–65.

[16] HOLMES, P., BERKOOZ, G. AND LUMLEY, J. (1996). *Turbulence, Coherent Structures, Dynamical Systems and Symmetry*. Cambridge Monogr. Mech., Cambridge University Press.

[17] ROWLEY, C., MEZIC, C., SCHLATTER, P. AND HENNINGSON, D. (2009). Spectral Analysis of Nonlinear Flows. *Journal of Fluid Mechanics*, **641**, 115–127.

[18] SCHMID, P. (2010). Dynamic mode decomposition of numerical and experimental data. *Journal of Fluid Mechanics*, **656**, 5–28.

[19] SCHMID, M. AND SATTELMAYER, T. (2011). Influence of Pressure and Velocity Perturbations on the Heat Release Fluctuations for Coaxial GH2/GO2 Injection. *4th*

European Conference for Aerospace Sciences, St. Petersburg, Russia.

[20] SCHMID, M. AND SATTELMAYER, T. (2012). Interaction of Acoustic Pressure Fluctuations with Supercritical Nitrogen Jets. *48th AIAA/ASME/SAE/ASEE Joint Propulsion Conference & Exhibit*, Atlanta, Georgia, USA, *AIAA 2012-3858*.

[21] RAMCKE, T., SCHMID, M. AND SATTELMAYER, T. (2013). Response Characterization of a LOX-GH2 Flame to Forced Acoustic Pressure Fluctuations. *5th European Conference for Aeronautics and Space Sciences, München, Germany*.

[22] WIERMAN, M., FELDMAN, T. AND ANDERSON, W. (2013). Development of Combustion Response Functions in a Subscale High Pressure Longitudinal Combustor. In: *49th AIAA/ASME/SAE/ASEE Joint Propulsion Conference & Exhibit*, San Jose, CA, *AIAA 2013-3778*.